Chinese Chemical Letters 37 (2026) 112357

Contents lists available at ScienceDirect

Chinese Chemical Letters

journal homepage: www.elsevier.com/locate/cclet

# Biomass-derived materials: Artful microstructure design and versatile applications

Yujia Zhao[a,1], Yingyi Li[b,1], Qingda An[b], Shuang Shan[c], Xianquan Li[a,c,*], Shangru Zhai[b,d,*]

[a] Chinese Academy of Science Key Laboratory of Science and Technology on Applied Catalysis, Dalian Institute of Chemical Physics, Chinese Academy of Sciences, Dalian 116023, China
[b] Liaoning Key Lab of Lignocellulose Chemistry and Biomaterials, Liaoning Collaborative Innovation Center for Lignocellulosic Biorefinery, College of Light Industry and Chemical Engineering, Dalian Polytechnic University, Dalian 116034, China
[c] State Key Laboratory of Catalysis, Dalian Institute of Chemical Physics, Chinese Academy of Sciences, Dalian 116023, China
[d] School of Environmental and Nature Resources, Zhejiang University of Science & Technology, Hangzhou 310023, China

ARTICLE INFO

*Article history:*
Received 15 June 2025
Revised 8 December 2025
Accepted 31 December 2025
Available online 31 December 2025

*Keywords:*
Biomass
Microstructure
Pollutant adsorption
Advanced oxidation process
Electromagnetic wave absorption

ABSTRACT

The properties of biomass-derived multifunctional materials have garnered increasing attention in the fields of environmental remediation, energy storage, and heterogeneous catalysis due to their abundant content of N and C, which can effectively modulate electronic structure and facilitate the anchoring of active centers. In this review, we summarized the progress of our team over the past decade on a variety of multifunctional materials with diverse morphologies, electronic structures, and geometric sites, developed through novel synthetic strategies that employ biomass and its derivatives as carbon sources. Those multifunctional materials exhibited excellent catalytic performance for the adsorption and degradation of pollutants in wastewater, absorption of electromagnetic waves (EMW), and photocatalytic reactions. Moreover, the underlying mechanisms of adsorption, degradation, and activation during the reaction process as well as the relationship between activity and structure are also discussed. This review offers comprehensive insights for fabricating biomass-derived materials, with a specific emphasis on their physicochemical properties characterized by controlled morphology, tunable electronic properties, and precise localization of active species, as well as the aspect of the intricate relationship between activity-structure and catalytic mechanisms, providing reference for future advancements in various catalysis fields involving biomass-derived materials.

© 2026 Published by Elsevier B.V. on behalf of Chinese Chemical Society and Institute of Materia Medica, Chinese Academy of Medical Sciences.

## 1. Introduction

The issues of energy and environment are of great global significance, thus there is an increasing urgency to explore renewable energy resources and cost-effective ecological remediation technologies [1,2]. The utilization of biomass or biomass-derived materials as precursors for the synthesis of hierarchical biochar has emerged as a prominent and globally recognized research field, primarily due to its inherent advantages in terms of sustainability, cost-effectiveness, eco-friendliness, and widespread availability [3,4]. Furthermore, the deliberate incorporation of active sites into these hierarchical carbon materials confers them with promising prospects in energy storage and conversion [5], heterogeneous catalysis [6], as well as environmental remediation [7].

The discharge of industrial wastewater, domestic sewage, noise pollution, sound waves, and solid waste poses a significant threat to human health in terms of environmental contamination [8]. Among these pollutants, the persistent refractory organic pollutants (POPs) and heavy-metal ions ($Pb^{2+}$, $Hg^{2+}$, $Cr^{3+}$, *etc.*) are of significant concern due to their limited degradability, irreversible nature, and high toxicity [9]. On the other hand, as technology and the electronics industry continue to rapidly advance, the deleterious effects of electromagnetic radiation are becoming increasingly conspicuous [10]. The graphene-based supported and doped catalysts not only possess the capability to effectively shield or absorb electromagnetic waves (EMW) but also demonstrate remarkable efficacy in achieving sewage purification and separation through advanced oxidation technologies (AOPs) [11,12], accordingly offering a potential solution to mitigate the current pollution crisis. However, the exorbitant cost and the intricate preparation process of

* Corresponding authors.
*E-mail addresses:* lixianquan@dicp.ac.cn (X. Li), zhaisrchem@163.com (S. Zhai).
[1] These authors contributed equally to this review paper.

https://doi.org/10.1016/j.cclet.2025.112357
1001-8417/© 2026 Published by Elsevier B.V. on behalf of Chinese Chemical Society and Institute of Materia Medica, Chinese Academy of Medical Sciences.

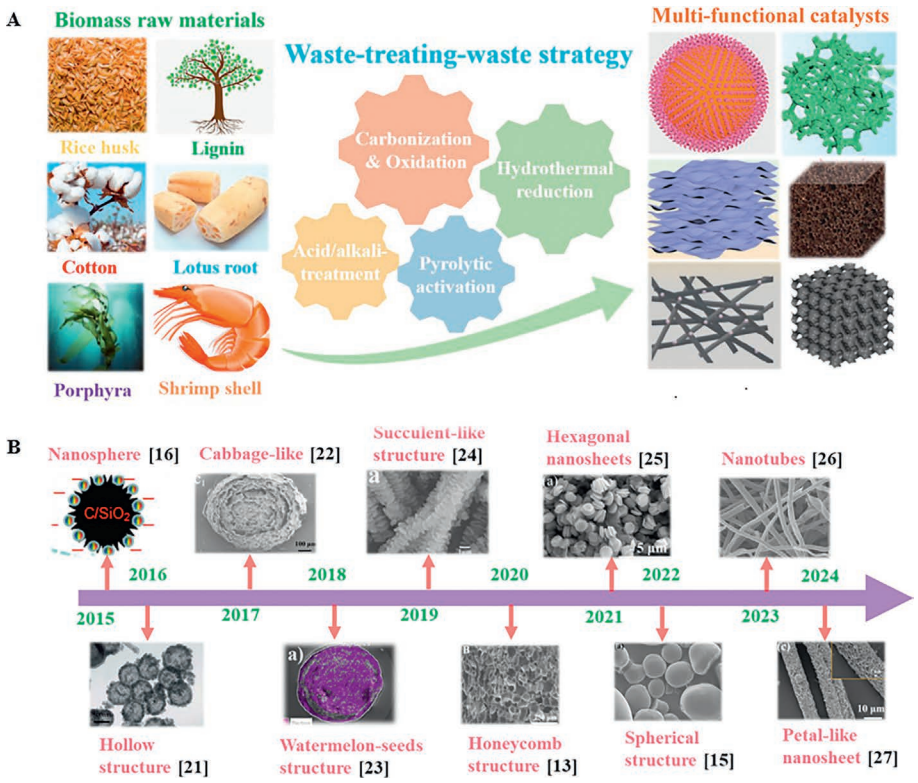



**Fig. 1.** (A) The illustration of the "waste-treating-waste strategy" for constructing multifunctional materials from biomass-derived sources, and (B) the representative biomass-based materials developed by our team over the past decade. Reproduced with permission [13,15,16,21–27]. Copyrights 2023, 2023, 2016, 2019, 2020, 2023 and 2024, Elsevier; 2016, RSC Royal Society of Chemistry; 2018, and 2024, American Chemical Society.

graphene impede the practical application of carbon-based materials in environmental remediation.

To tackle the challenge of expensive catalysts, we have devised a "waste-treating-waste strategy" to obtain multifunctional carbon materials derived from waste biomass, including fruit shells [13], shrimp shells [14], lotus roots [15], rice husks [16]. To be specific, the desired morphology and topological structure of biochar through a series of processes, starting with pyrolysis carbonization of biomass materials, followed by subsequent treatments such as hydrothermal reduction and acid-base modification, as illustrated Fig. 1A. After the biochar undergoes post-treatment with a surface modification process, the carboxyl, amino, and hydroxyl species are newly formed. This not only enhances the effective anchoring of active metals but also facilitates the modulation of electronic properties and coordination environment towards the active sites. The assembled integrated multi-functional catalyst enables the selective adsorption of toxic metals and plays a pivotal role in facilitating the rapid generation of reactive oxygen species (ROSs) and efficient oxidation of POPs (carbamazepine (CBZ), bisphenol A (BPA), tetracycline (TC), sulfadiazine (SDZ), *etc.*).

This review presents our research group's decade-long development of the "waste-treating-waste" concept, which involves harnessing agricultural or forestry waste as raw materials to synthesize versatile biochar catalysts for sewage treatment and EMW degradation. First, our focus lies in the development of synthesis strategies such as molecular self-assembly, mesoscopic morphology control, and electronic tunability to fabricate biomass-derived multifunctional materials with controlled properties in terms of morphology and chemical electronic state, by regulating metal ions, surfactants, nitrogen carbon content, chelating agents, and preparation conditions. The constructed catalyst, featuring diverse mesoscopic morphology and metal active sites localization, has achieved selective adsorption of heavy metal ions and dyes in wastewater while elucidating the underlying mechanism of adsorption. Notably, the Co-NC catalyst, which combines molecular self-assembly and mesoscopic morphology control strategies, demonstrates superior catalytic performance in the degradation of antibiotics, and the proposed degradation pathway is unveiled through a combination of diverse energy spectra and spectroscopic techniques. Subsequently, the high entropy alloy catalysts constructed through electronic control strategy demonstrates excellent EMW absorption ability, and the mentioned electromagnetic attenuation mechanism provides a theoretical basis and feasible strategy for the practical application of electromagnetic functional devices, such as ultra-wideband bandpass filters. In addition to the biomass-derived catalysts, the fabrication of a heterointerface between lignin and graphene catalyzes the molecular oxygen to hydrogen peroxide ($H_2O_2$) reaction, providing a promising strategy for developing high-performance photocatalysts based on lignin. Finally, the recent challenges and prospects for the future synthesis and preparation of biomass-derived materials, as well as the molecule-level microscopic mechanisms in various applications, are proposed.

## 2. Design and construction of biomass-derived materials

Currently, the predominant methods for synthesizing biochar-based catalysts include: (1) Direct carbonization, (2) template-assisted synthesis, (3) hydrothermal carbonization, and (4) activation-pretreatment process [4,17–20]. The various arrangements and combinations of the aforementioned methods facilitate the acquisition of biomass-derived materials with artful structures and functions, thereby enabling their utilization in energy storage, adsorption, wave absorption, and catalytic conversion processes. Herein, we have developed a range of multifunctional materials derived from agricultural or forestry waste biomass through the implementation of strategies for precise control over mesoscopic

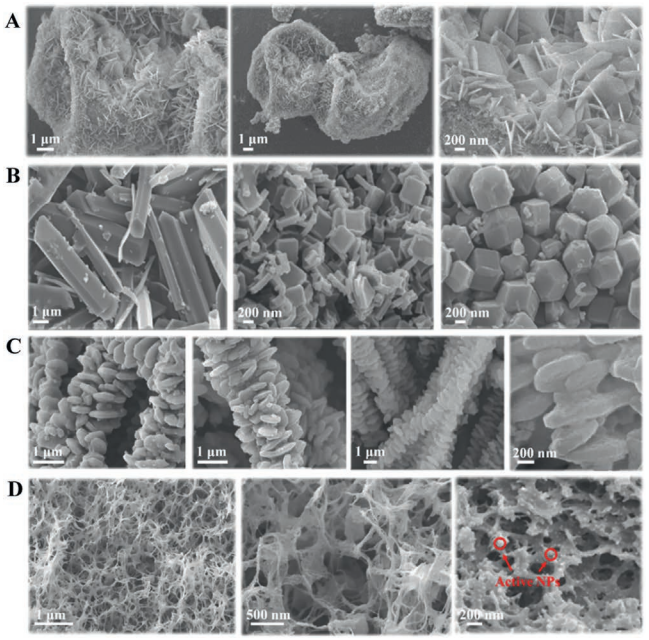



**Fig. 2.** (A) SEM images of the FeNi/LSC-700. Reproduced with permission [32]. Copyright 2024, Springer. (B) SEM images of NC-R, NC-OP and NC-RD. Reproduced with permission [33]. Copyright 2024, Elsevier. (C) SEM images of Co-NCL@ZrSBA-15. Reproduced with permission [24]. Copyright 2020, Elsevier. (D) Co/N@ZS-SA catalyst. Reproduced with permission [39]. Copyright 2021, Elsevier.

morphology, electronic tunability, and molecular self-assembly in recent decade as shown in Fig. 1B [13,15,16,21–27].

### 2.1. Mesoscopic morphology control strategy

Generally, the surface topography control strategies can be broadly classified into two main approaches: the top-down hard template strategy and the bottom-up soft template strategy [3,17–20]. Numerous studies have demonstrated the effectiveness of the top-down hard template method in tailoring the morphology of biomass-derived materials. For instance, Yu *et al.* [28] utilized ZIF-8 as a volatile hard template and Litsea cubeba leaves as a carbon source, successfully fabricated a highly dispersed and hierarchical porous biochar. Wang *et al.* [29] developed a green strategy using KCl as the sole hard template for the fabrication of porous biochar SK-C (Fig. S1A in Supporting information). He *et al.* [30] employed a soft-hard template method to create N/S co-doped biochar from shrimp shell waste, providing hierarchical porous structure and more active sites, which effectively degraded sulfadiazine through a non-radical pathway. Zhu *et al.* [31] used calcium citrate tetrahydrate (CCT) as a hard template and $K_2CO_3$ as an activator to tailor the pore structure of bio-oil, synthesizing a hierarchical biochar CCT-700-1:2 with a remarkably high specific area of 2213.09 $m^2/g$ (Fig. S1B in Supporting information). Recently, our group employed a biomass-derived carbon or the derived MOF framework as a hard template for the fabrication of multifunctional materials with specific morphologies. As illustrated in Fig. 2A, the sponge-like structure FeNi alloy nanosheet arrays were synthesized using a facile hydrothermal method [32], employing highly porous and hollow structures of Lycopodium spores as the biomass-derived carbon template. Furthermore, a series of paper-like membranes (Fig. 2B) featuring rod, octagonal plate, and rhombic dodecahedron morphological structures were successfully fabricated by combining MOF with interwoven cellulose nanofibrils [33], with remarkable hydrophilicity, stability, and photothermal conversion capabilities.

Except for the top-down method, researchers have also employed the bottom-up soft template strategy to control the mesoscopic morphology of biomass-based materials. For example, Wang *et al.* [34] fabricated a one-dimensional hollow KCF material from kapok fibers and coated it with two-dimensional hydrangea-like $MoS_2$ using a carbonization and hydrothermal method (Fig. S1C in Supporting information). Li *et al.* [35] developed a facile soft-template carbonization strategy to fabricate tunable carbon superstructures (spherical/rod-like/shell-like) using PSSMA as the structure guiding agent, where the optimized shell-like architecture achieves superior microwave absorption through hierarchical porosity and enhanced dielectric loss (Fig. S1D in Supporting information). Ni *et al.* [36] designed a rail-like hetero-structured $V_2O_3$@C/BWs derived carbon from butterfly wings and exhibited high performance in EMW. Our group also developed an inducible soft-to-hard templating idea to finely tune the morphology and pore structure by employing sodium alginate crosslinking with $Ca^{2+}$ ions [37]. Furthermore, the Si-OH generated through the utilization of P123 as a soft template agent and tetraethyl orthosilicate (TEOS) as a silicon source readily anchors metal active center (*e.g.*, Co, Cu, and Fe) [38], thereby facilitating the fabrication of functional materials possessing well-defined pore structures and specific coordination microenvironments. As a result, we successfully obtained hierarchical succulent-like Co-NCL@ZrSBA-15 (Fig. 2C) and mesoporous composite hydrogels doped with Co/N(Co/N@ZS-SA) (Fig. 2D) [24,39].

### 2.2. Electronic modification strategy

The utilization of doping agents (N, S, P, *etc.*) or the incorporation of secondary metals to regulate the d-electron center structure of active metals has emerged as the predominant approach for electronic modification strategies [40,41]. Biomass-derived materials offer ample nitrogen sources that can be accurately adjusted under various atmospheres (*e.g.*, nitrogen, oxygen mixtures, and air) to create a microenvironment structure with diverse coordination modes between central atoms and nitrogen, thereby enhancing ability in environmental remediation. For example, the 3D hierarchical carbonaceous aerogels, embedded with honeycomb-like carbon/bimetallic sulfide and oxide nanoparticles, demonstrate an enhanced dielectric loss upon N-doping, leading to superior performance for supercapacitors [42]. Tang *et al.* [43] synthesized a graphene-like Enteromorpha biochar modified g-$C_3N_4$ (BC/CN) with a tunable band structure, demonstrating efficient photocatalytic degradation of multiple antibiotics including ciprofloxacin (CIP), oxytetracycline (OTC), pefloxacin (PFLX), levofloxacin (LVFX) and pefloxacin (PFLX). Guo *et al.* [44] developed a 3D hierarchical porous carbon derived from nitrogen-rich egg white, loaded with $Fe_3O_4$ nanoparticles ($Fe_3O_4$@AEWC). The enriched N atoms in the carbon matrix optimize dielectric properties by introducing polarization centers (*e.g.*, C-N dipoles, pyridinic-N defects) and improving impedance matching (Fig. S2A in Supporting information).

Sulfur is also known as an efficient dopant for inducing effects. Wang *et al.* [45] utilizes waste ginkgo leaves to prepare S/N self-doped biochar as a bifunctional cathode catalyst (WLGC-800), achieving efficient $H_2O_2$ generation and organic pollutant degradation, demonstrating excellent electrochemical performance and practical application potential (Fig. S2B in Supporting information). Similarly, our group developed a S-doped sodium carboxymethyl cellulose derived 3D hierarchical porous carbon $Cu_xS$@S-CPC (as depicted in Fig. 3A), facilitating effective ion diffusion pathways and enhancing charge transfer for Faradaic redox reactions due to its excellent electron conduction at the interface and remarkable redox activity of $Cu_xS$ particles [46]. Furthermore, a $Ni_3S_2$@S-PFPC material was fabricated by uniformly dispersing $Ni_3S_2$ onto S-doped passionfruit peel-derived porous carbon (S-PFPC) [13], ac-

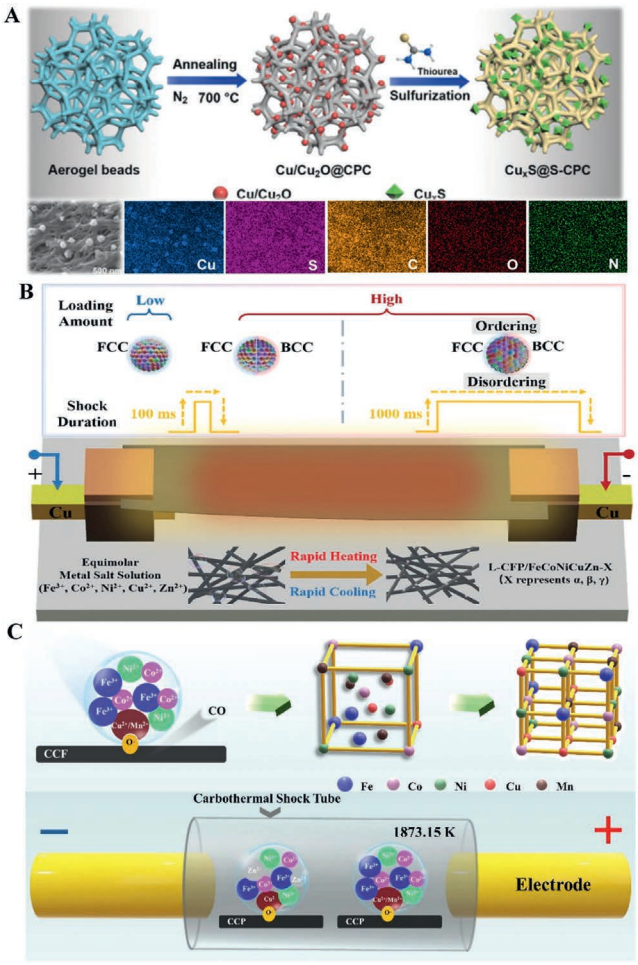



**Fig. 3.** (A) The synthesis scheme of $Cu_xS$@S-CPC and its corresponding SEM mapping. Copied with permission [46]. Copyright 2023, Elsevier. (B) The schematic illustration of synthesis process of the L-CFP/FeCoNiCuZn. Reproduced with permission [48]. Copyright 2024, Wiley. (C) The synthesis protocol of CCP/FeCoNiCuMn HEAs using the carbothermal shock method. Reproduced with permission [49]. Copyright 2024, CC BY-NC-ND 4.0.

counting for higher charge storage capacity by enhancing electron transport in our recent work.

Phosphorus doping has also shown significant potential in modifying the properties of biomass-derived materials. Tan *et al.* [47] combined 3D-printed multi-scale EMW modulation with material/structural dispersion engineering to achieve ultra-wideband and wide-angle microwave absorption, where atomic-scale phosphorus doping in stabilized carbon skeletons strategically leverages defects and vacancies to optimize dielectric properties (Fig. S2C in Supporting information). The manipulation of geometric distance and coordination environment between metals represent a commonly employed strategy for modulating the energy barrier of the d-band, which is closely associated with catalytic activity during the reaction process [7]. In our recent work, Cu and Zn were utilized as electron-rich centers on the FeCoNiCuZn HEA nanoparticles immobilized onto lignin-based carbon fiber paper (L-CFP/FeCoNiCuZn-X) through the carbothermal shock method, with precise control of element loading amount, shock temperature, and duration (as illustrated in Fig. 3B) [48]. The tunable electron-rich active centers function as intermediate stations for electron migration, facilitating the transfer of electrons to L-CFP/FeCoNiCuZn HEA heterointerfaces and endowing a high level of EMW absorbing efficiency [48]. Subsequently, another CCP/FeCoNiCuMn HEAs with shell-core heterointerfaces also possessing superior EWA absorbance performance by the enhanced electron migration mode of switchable electron-rich active sites, which are modified using the reformative carbothermal shock method and incorporate varying amounts of Mn (Fig. 3C) [49].

### 2.3. Molecular self-assembly strategy

The functionalization of biomass-derived materials through tailored chemical modifications markedly improves their physicochemical properties, such as optimizing surface chemistry, refining pore structure, enhancing mechanical stability, and boosting reactive site density. Consequently, these materials exhibit exceptional adsorption capacity and broader application versatility in environmental remediation. The functional groups (such as hydroxyl, amino, and carboxylic moieties) of biomass can engage in non-covalent interactions with active metals through molecular self-assembly method, leading to the formation of multifunctional materials through various mechanisms including hydrogen bonding, host-guest interactions, metal coordination chemistry, $\pi$-$\pi$ stacking interactions and charge transfer phenomena [50]. For instance, Wang *et al.* [51] synthesized amino/hydroxyl-functionalized Fe/Ni-biochar composites (FeNi-RSN-(OH)($NH_2$) and FeNi-RSN-OH), achieving 4.3–4.8 times higher Pb(II)/Cd(II) adsorption (242.15 and 229.52 mg/g) than raw biochar, driven by –$NH_2$/–OH-enhanced complexation, electrostatic interactions, and ion exchange. Qi *et al.* [52] utilized oxygen-, nitrogen-, and phosphorus-containing groups to functionalize MgO-loaded fish scale biochar (MgO-FB), exhibiting exceptional adsorption capacities ($Cu^{2+}$: 505.8, $Cd^{2+}$: 327.2, $Pb^{2+}$: 661.2 mg/g) through MgO-enhanced ion exchange/precipitation and HAP dissolution. Abundant functional groups (hydroxyl, carboxyl, phosphate) synergistically improved metal binding *via* complexation and $\pi$-electron coordination, while demonstrating superior soil remediation efficacy (84.2 % Cu, 74.2 % Cd immobilization) (Fig. S3A in Supporting information). In our recent study, we employed diethylenetriamine for the modification of lignin *via* a Mannich reaction, resulting in the formation of aminated lignin [53]. This facilely facilitates the anchoring of zirconium components onto the $NH_2$ group within the lignin framework and enables the efficient and environmentally friendly capture of phosphate using a sustainable bio-sorbent (AL-DETA@Zr) (Fig. S3B in Supporting information) [53]. Additionally, the hydroxyl and amino groups in goat manure effectively facilitate the binding of $Co^{2+}$ species through cross-linking and chelation (Fig. S3C in Supporting information), enhancing the interactions between cobalt nanoparticles and the graphitized biochar network, thus improving the stability of the Co-GMC-900 catalyst [54].

Apart from biomass raw materials, we have designed newly developed $CoS_2/Cu_2S$ embedded N/S co-doped mesh carbon matrix composites with three-dimensional mesh-like structures (Fig. S3D in Supporting information), formed through the strong interaction between metal active species and carboxymethyl cellulose's hydrogen bonding hydroxyl group (a derivative of biomass) [55]. The sodium alginate (SA) is crosslinked with melamine (Me) through hydrogen bonding between the carboxyl group (-COOH) and the amino group (-$NH_2$), while $Ca^{2+}$ forms an interconnected Ca-Me/SA polymer network *via* chemical bond interactions (H···N, O-O, -COO-Ca-OOC-). Afterwards, the hydrogen bond between -COOH and the N-containing component in SA is converted into a more robust chemical bond through the crosslinking action of glutaraldehyde in a weakly alkaline system containing polyvinylimide (PEI), leading to the formation of a three-dimensional network precursor Ca-Me/SA@0.75PEI (Fig. S3E in Supporting information) [23]. The surface chelating sites were effectively increased through this process, thereby facilitating the successful self-assembly of Co nanocrystals into a watermelon-like structure as shown in Fig. S3E [23]. In addition, the hollow nanotube-like polypyrrole was syn-

thesized using a "self-aggregation assembly" strategy, relying on the utilization of methyl orange and ammonium persulfate as templates and oxidants as shown in Fig. S3F (Supporting information) [56], respectively. Finally, we fabricated a novel nanotube-like composite core-shell of PPy@$MoS_2$ through the utilization of chemical oxidative polymerization followed by hydrothermal reaction, resulting in the formation of hollow PPy nanotubes as the core and intertwined $MoS_2$ nanosheets as the outer shell [56].

In summary, various preparation methods for biomass-derived catalysts, including hard and soft templating, electronic modification, and molecular self-assembly strategies have been concluded herein this review. Each method offers unique advantages in tailoring the microstructure and electronic properties of the resulting materials. Hard and soft templating approaches allow for precise control over pore structures and morphologies, creating hierarchical porous materials that enhance adsorption and catalytic performance. Electronic modification through doping or metal incorporation effectively adjusts the electronic characteristics of biomass-derived materials, thereby modulating the d-electron center structure of active metals and improving their activity in redox reactions and electromagnetic wave absorption. Molecular self-assembly utilizes the inherent functional groups of biomasses to create complex, well-ordered structures with rich active sites. These diverse preparation methods provide a robust foundation for the design and development of biomass-derived catalysts with tailored properties for specific applications in environmental remediation, energy storage, and beyond. The continuous exploration and optimization of these methods will further advance the performance and practical applicability of biomass-derived catalysts, paving the way for sustainable solutions in various fields.

## 3. Versatile applications of the biomass-derived materials

In this section, we will introduce versatile application of multifunctional catalysts derived from biomass in our recent work over the past decade. The applications encompass pollution adsorption, pollution degradation, EWA, as well as catalytic conversion processes, as shown in Tables S1-S3 (Supporting information).

### 3.1. The practical application of pollution adsorption

Owing to cost-effectiveness, sustainability, and high efficiency, biomass-based materials have emerged as promising adsorbents for removing heavy metal ions. With adjustable surface chemistry, high adsorption capacity, and eco-friendliness, biomass materials present a sustainable solution to environmental pollution challenges [57–60]. Recent studies have demonstrated remarkable advancements in this field. For instance, rice husk biochar doped with deep eutectic solvent and $Fe_3O_4$/ZnO nanoparticles was reported a maximum adsorption capacity of 384.62 mg/g for Pb(II), showcasing the potential of functionalized biochar composites [61]. Hao *et al.* [62] highlighted the effectiveness of MgO-loaded S-doped porous biochar composites, which achieved impressive adsorption capacities of 630 mg/g for Cd(II) and 2022 mg/g for Pb(II) in single-metal systems. Tian *et al.* [63] found that co-doping of Si-Mg can enhance surface area and oxygen-containing groups, boosting the capacity of ion exchange, reaching an maximum adsorption capacity of 1185.91 mg/g for $Cd^{2+}$. Zhang *et al.* [64] synthesized a novel biochar@chitosan-polyethyleneimine composite (BC@CSPTI), which achieved a remarkable static saturated adsorption capacity of 633.4 mg/g for uranium(VI), through the synergistic effects of minerals and functional groups, and demonstrated high stability. Fan *et al.* [65] developed a functionalized cotton charcoal/chitosan biomass-based hydrogel (CS/EDTA/CBC), which demonstrates exceptional adsorption capacities for $Pb^{2+}$, $Cu^{2+}$, and methylene blue (MB) of 1105.78, 678.04, and 590.72 mg/g respectively, along with remarkable reusability and stability, making it a promising adsorbent for efficient removal of heavy metal ions, and dyes from wastewater.

Building on these advancements in biochar engineering, our work demonstrates the practical translation of agricultural waste into high-performance adsorbents. Rice husk (RH-c), primarily composed of cellulose (40 %-50 %), hemicellulose (25 %-30 %), and lignin (15 %-20 %) with ~20 % silica [16], serves as an ideal precursor for functional material development through targeted modifications. Introducing specific functional groups such as carboxyl, amino, and cyclodextrin enables chemical modifications of these components, resulting in the development of high-performance functional materials for targeted adsorption of pollutants from aqueous systems (Fig. 4A) [16]. We have developed a novel multifunctional bio-adsorbent, namely RH-c/$Fe_3O_4$/CD, by synergistically combining low-temperature solution carbonized RH-c, $\beta$-cyclodextrins ($\beta$-CD), and $Fe_3O_4$. As illustrated in Fig. 4B, the equilibrium isotherms for the adsorption of MB over the catalysts indicate a preference for fitting the Langmuir isotherm model rather than Freundlich isotherm models, with the adsorption kinetics conform to *pseudo*-second-order models. The value of RL $<$ 1 can be observed from Fig. 4B, indicating the favorable adsorption of the MB over the catalyst. This can be attributed to formation of hydrogen bonds between MB and hydroxyl groups on the surface of CD, as well as oxygen-containing functional groups on the composite's surface [16]. In consideration of the magnetic and highly recyclable properties exhibited by RH-c/$Fe_3O_4$/CD material, a novel magnetic catalyst, AL-$NH_2$@$Fe_3O_4$-Ce [66] was synthesized *via* the Mannich reaction followed by the chemical coprecipitation method. The catalyst demonstrated enhanced affinity and tailored interfacial chemistry for targeted phosphate removal, along with its exceptional recycling capability during five consecutive cycles, and followed a Langmuir model adsorption isotherm and the adsorption kinetics adhered to the *pseudo*-second-order model [66].

Given the prevalence of hazardous heavy metal ions, such as Cd(II) and Cr(VI), in industrial wastewater, we have developed a novel highly efficient and cost-effective adsorption catalyst, CMC/CS/PDA@PEI, demonstrating high adsorption capacity and fast sorption kinetics for removing Cd(II) and Cr(VI) from aqueous solutions [67]. This notably absorbent material was synthesized from carboxyl methylcellulose and chitosan, involving self-polymerization of chitosan and dopamine, followed by doping in sodium carboxymethyl cellulose and cross-linking with glutaraldehyde. Fig. 4C depicts the kinetic models of cadmium and chromium ion adsorption on the CMC/CS/PDA@PEI catalyst, specifically the *pseudo*-second-order and *pseudo*-first-order models [67]. The adsorption mechanism of heavy metal ions on CMC/CS/PDA@PEI involves a synergistic effect between amino and carboxyl groups, with a slight difference observed between Cd(II) and Cr(VI). On the one hand, the cadmium adsorption mechanism (Fig. 4C) [67] involves the coordination of empty d-orbitals of cadmium with nitrogen-containing or oxygen-containing groups, leading to the formation of cadmium ions through coordination bonding and chelation on the CMC/CS/PDA@PEI catalyst, specifically with carboxyl and amine groups. On the other hand, the hexavalent chromium, characterized by its high electronegativity, initially undergoes adsorption through electrostatic interaction with protonated amine groups. Subsequently, it is reduced to trivalent chromium and absorbed onto the CMC/CS/PDA@PEI catalyst containing oxygen-containing and nitrogen-containing groups under acidic conditions. The adsorption mechanism of Cr(VI) species onto the Alg-CB-X catalyst (Fig. 4D), derived from alginate, is consistent with our previous research [68]: (1) Initially, the transfer of Cr(VI) species from the external environment to the material surface occurs through strong electrostatic interactions between negatively charged $HCrO_4^-$ species and protonated oxygen-containing

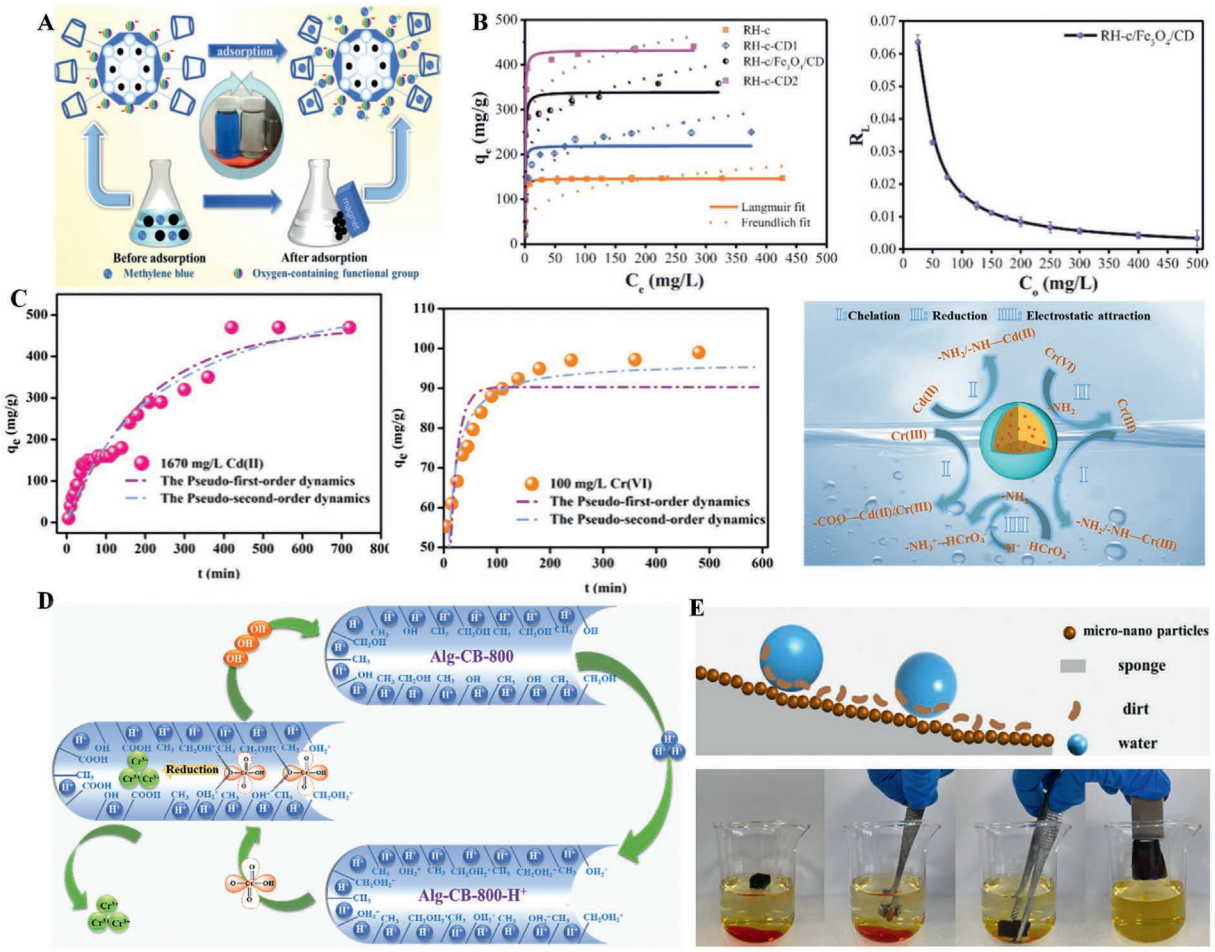



**Fig. 4.** (A) Schematic depiction of the synthesis procedure for multifunctional RH-c/$Fe_3O_4$/CD and (B) its absorbance performance in MB. Copied with permission [16]. Copyright 2016, Elsevier. (C) The adsorption model of CMC/CS/PDA@PEI for Cd(II) and Cr(VI) and the illustration of adsorption mechanism. Copied with permission [67]. Copyright 2020, Elsevier. (D) The possible mechanism of Alg-CB-X for Cr(VI) removal. Reproduced with permission [68]. Copyright 2023, Elsevier. (E) The illustration of separation of oil and water. Copied with permission [70]. Copyright 2016, Royal Society of Chemistry.

functional groups. (2) Subsequently, Cr(VI) ions permeate into the internal pores of carbon beads where a portion undergoes reduction by C–H or C–OH groups. (3) Finally, the carbon surface acts as a deposition site for Cr(VI), while resulting in subsequent release of Cr(III) into the external environment due to electronic repulsion between Cr(III) species and positively charged group.

In addition to their aforementioned capabilities in adsorbing dyes, antibiotic pollutants, and heavy metal ions in water, biomass-based materials also possess the ability to achieve efficient oil-water separation. A novel composite of PDMS (polydimethylsiloxane)/magnetic lignin particles (lignin@$Fe_3O_4$)/PDA sponge magnetic micro-nano super-hydrophobic surfaces was fabricated through the self-polymerization of dopamine (DA), covalent deposition of magnetic lignin (ML), and PDMS silane modification [69]. As shown in Fig. 4E, the as-prepared material exhibited remarkable efficiency in the separation of oil and water, enabling effortless magnetic retrieval. Furthermore, it demonstrated exceptional water resistance even after undergoing 10 consecutive extrusion processes (Fig. 4E), owing to the "lotus effect" resulting from the rapid self-healing of contaminant damage caused by adhesion to its super-hydrophobic interface [70].

### *3.2. The practical implementation of pollutant substance degradation*

Biomass-based materials have also emerged as sustainable and cost-effective catalysts or supports for AOPs in recent years. These materials offer several advantages, including high surface area, porosity, and abundant surface functional groups that can be tailored for specific applications with a rather low cost. Metal-free biochar catalysts, for instance, are capable of activating oxidants like persulfate (PS) through electron transfer pathways mediated by surface functionalities [43,71–74]. Li *et al.* [75] developed a low cost corn straw-derived biochar (CBC) for the activation of peracetic acid (PAA) in TC degradation *via* electron transfer mediated by carbonyl groups, demonstrating high practical applicability with good recyclability and adaptability to different pollutants. Similarly, Dou *et al.* [73] also utilized B/N co-doped biochar for the degradation of TC where B and N atoms not only enhanced the activation of peroxydisulfate (PDS) but also shifted the oxidation mechanism from a conventional radical-based process to a non-radical one. As shown in Fig. 5A, DFT calculations elucidate the underlying mechanism by quantifying the narrowed band gap and enhanced electron transfer from pollutant HOMO to PDS* LUMO, validating the potential difference-driven electron transfer pathway [16]. Qu *et al.* [74] developed a nitrogen-rich pinewood biochar NKBC800, further highlighted the role of pyridinic nitrogen in PMS activation for the degradation of CIP.

Transition metal catalysts (Co, Fe, Ni, *etc.*) was widely used in AOPs due to their high efficiency and recyclability [76–81]. However, the high tendency of leaching limited their applications. As a promising support with high surface area, biochar can effectively immobilize the metals to avoid leaching with enhanced catalytic

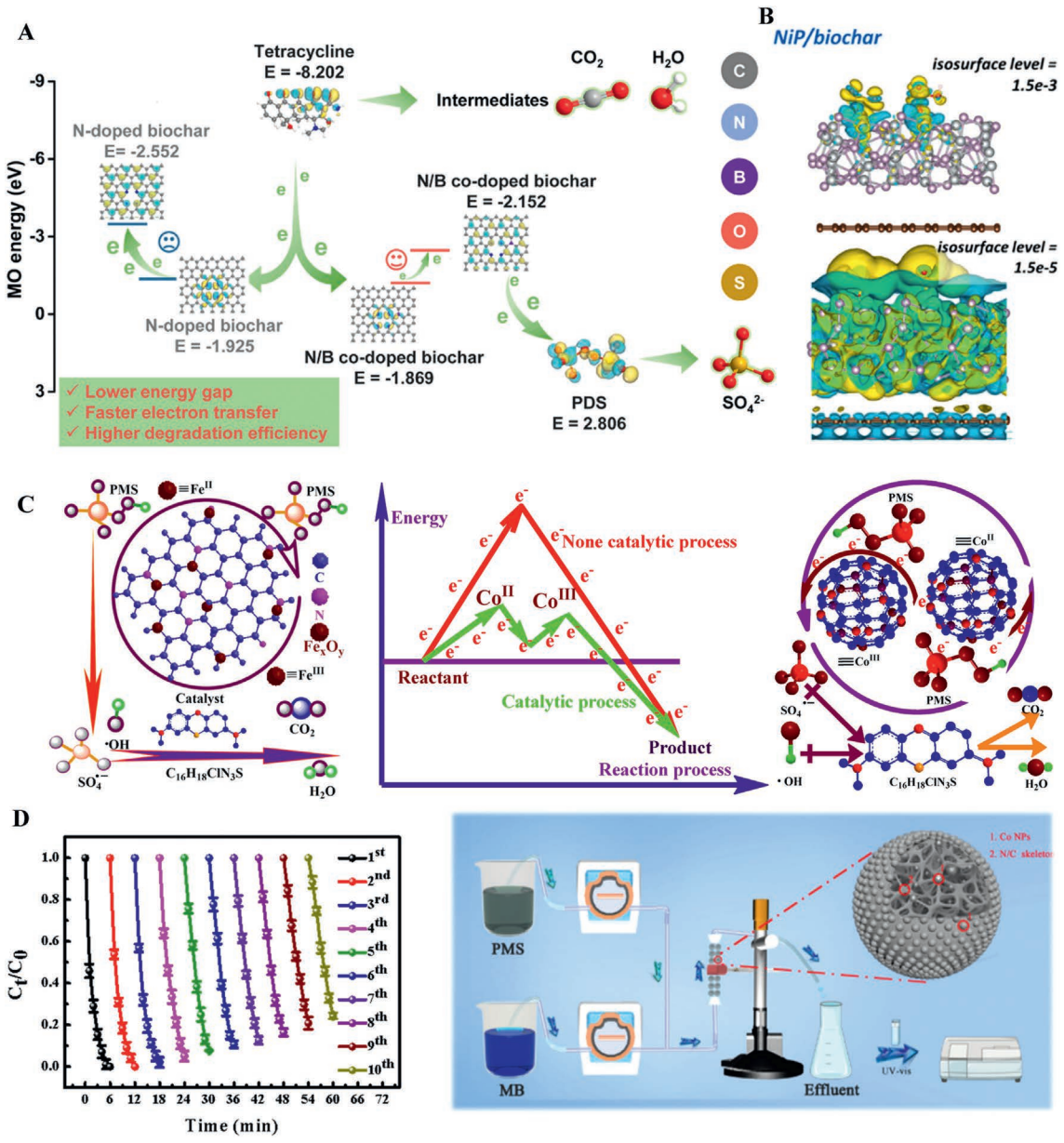



**Fig. 5.** (A) The adsorption of PDS on B/N biochar and the electron-transfer pathways driven by potential energy difference for TC oxidation. Copied with permission [73]. Copyright 2024, Elsevier. (B) Adsorption and activation of $S_2O_8^{2-}$ by $Ni_xP$/biochar composite with the corresponding charge density differences. Copied with permission [86]. Copyright 2024, Elsevier. (C) Mechanism of the degradation pathway over $Fe_xO_y$/N-GN/CNTs and SA/N-$Co_xO_y$-X catalyst. Copied with permission [12,87]. Copyrights 2018, Elsevier. (D) The recyclability of the Co-NC-0.25-700 catalyst in the continuous flow experiment. Copied with permission [88]. Copyright 2019, CC BY-NC-ND 4.0.

performance. For example, Co-doped biochar systems, such as kelp-derived Co-N/KC-900 [82] and pomelo peel-based Co/BDPPF [83], achieved rapid antibiotic removal (>99 % in 15 min) *via* PMS activation, with minimized metal leaching. Iron-biochar composites, including ZVI/BC [84] and Fe@N-BC [77], demonstrated robust performance in degrading sulfadiazine (SDZ) and lindane, with stable pH adaptability. Notably, Liu *et al.* found that pre-reduction strategies in Fe-biochar systems [85] enhanced PMS activation through synergistic $Fe^{2+}$/hydroxyl group accumulation. Wang *et al.* [86] utilized phytic acid for the modification of $Ni_xP$/biochar composite, achieving 94.6 % TC removal within 180 min and exhibiting low Ni leaching. DFT results demonstrated that biochar elevated the Ni 3d-band center and lowers the work function, strengthened PS adsorption, and synergistically promoted electron donation from Ni, P, and C to induce surface-bound $SO_4^{\bullet-}$ formation and subsequent radical chain reaction, as shown in Fig. 5B.

To synergize the advantages of both transition metal and nonmetal modified biochar, our research group have been focusing on strategically integrate Fe/Co species into biomass-derived carbons for the degradation of water pollutants, such as organic dyes and antibiotics through AOPs. For instance, in addressing the degradation of organic model pollutant like MB, we fabricated a three-dimensional multifunctional heterostructure catalyst ($Fe_xO_y$/N-GN/CNTs), which efficiently degraded MB within 12 min at a concentration of 100 mg/L [12]. The notably catalytic performance can be ascribed to the synergistic interaction between pyridine nitrogen and iron oxides, leading to a substantial generation of $SO_4^{\bullet-}$ and $^{\bullet}OH$ radicals (Fig. 5C) [12]. Subsequently, the designed SA/N-$Co_xO_y$-X catalyst featuring a core-shell structure synthesized *via* the molecule self-assembly method, not only rapidly degrades MB but also effectively degrades other pollutants like *p*-nitrophenol and tetracycline [87]. As depicted in Fig. 5C, the under-

lying reason lies in the Co-N species constructed within this catalyst, which facilitates facile electron transfer between $Co^{2+}$ and $Co^{3+}$ species, thereby effectively activating PMS to generate free radicals [87]. Based on this foundation, we further enhanced the confinement effect of the unique "egg box" structure in the Co-NC-0.25-700 catalyst by optimizing the coordinated environment of Co-NC, thereby significantly improving the cyclic stability (Fig. 5D) of Co species leaching [88]. The application potential of the designed catalyst was demonstrated through continuous flow degradation of organic matter in a fixed bed reactor, achieving over 90 % MB degradation within 200 min and demonstrating capability for degradation up to 260 min, which represents significant progress towards the practical implementation of AOPs (Fig. 5D) [88]. The newly formed Co-NC species not only enhance the adsorption capacity for $HSO_5^-$ and disrupt the O-O bond (HO-$SO_4^{\bullet-}$) compared to Co-N species, but also facilitate electron transfer from adjacent carbon atoms to nitrogen atoms. This accelerates $Co^{2+}/Co^{3+}$ species recycling, thereby expediting the production of $SO_4^{\bullet-}$ and $^{\bullet}OH$ and promoting production of $SO_4^{\bullet-}$ and $^{\bullet}OH$ and promoting MB degradation, in consistent with those reported previously [89,90].

Considering the superior catalytic performance of Co-NC in the degradation of MB, we further synthesized Co/NC materials with diverse microstructures using nitrogen and carbon-rich biomass sources such as goat manure and shrimp shells, and employed them for the degradation of CIP, a challenging antibiotic to degrade. The Co-GMC-900 composite, derived from the carbonization of cobalt-impregnated goat manure, endowed high performance in activating PMS for CIP removal, resulting in a degradation efficiency of 96.5 % within a 30-min timeframe [54]. Subsequently, the cobalt-based biochar (Co-SSP-700) is synthesized through the synergistic interaction between *in-situ* $CoSiO_x$ and the abundant oxygen-containing functional groups of natural marine shrimp shells, (rich in N, C, and Si), also showed remarkable degradation performance towards CIP (Fig. S4A in Supporting information) [14]. The notably high degradation efficiency can be attributed to the combined effect of radical processes ($SO_4^{\bullet-}$, $^{\bullet}OH$, and $O_2^{\bullet-}$) generated by the $Co^{2+}/Co^{3+}$ species activating PMS (Fig. S4B in Supporting information), in conjunction with non-radical processes ($^1O_2$ and charge transfer) originating from graphite carbon and unsaturated oxygen-containing functional groups (*e.g.* -COOH, -C=O, and -COO-) resulting from inherent heteroatom doping of biochar [14,91–94].

The biochar crops, such as cotton, lotus root, and porphyra, contain trace amounts of elements like phosphorus (P) and sulfur (S), which further regulate the electrochemical center of the active metal, facilitating the efficient activation of PMS for rapid degradation of pollutants. The Co-CCF-600, a 3D hollow tubular composite composed of cobalt and carbon fibers derived from cotton, was synthesized through the process of carbonization [26]. This resulted in a degradation rate of 93.47 % for CBZ within a duration of 60 min, which remained at 95.10 % even after continuous operation for 300 min (Fig. S5A in Supporting information) [26]. Furthermore, the initial 60-min period achieved a 50 % removal of CBZ, and the catalyst exhibited consistent CBZ removal efficiency of 61.57 % after 118 h, showcasing remarkable degradation efficacy and stability with promising practical applications [26]. On the one hand, the presence of the $Co^0$ species facilitates the redox cycle of $Co^{2+}/Co^{3+}$ (Fig. 6A), thereby enabling a continuous generation of $SO_4^{\bullet-}$ and $^{\bullet}OH$, playing a crucial role in CBZ degradation [26]. Besides, the carbonyl groups (C=O) and hydroxyl groups (−OH) undergo electron transfer with PMS, leading to the generation of $^1O_2$, which also contributes significantly to the degradation process of CBZ. However, the non-free radical pathway ($^1O_2$) (Fig. 6B) predominantly governs the degradation of CBZ over the Co-CA-900 catalyst derived from lotus root due to its lower charge transfer resistance ($R_{ct}$), improved electrochemical impedance, reduced Warburg impedance, and enhanced ion diffusivity in electrolytes (Figs. S5B(a) and (b) in Supporting information) [15]. As shown in Fig. S5B(c) (Supporting information), the interaction between Co-CA-900 and PMS results in the formation of a metastable complex, attributed to the augmentation of the open circuit potential upon PMS addition [15]. In addition, the presence of a C=O structure on the Co-CA-900 catalysts can induce the generation of $^1O_2$ and enhance the activation of PMS [15]. Moreover, the linear correlation (Fig. S5B(d)) between the content of C=O and the reaction rate constant, providing further evidence for the involvement of a non-radical oxidation pathway in this process [15].

The prominent role of singlet oxygen ($^1O_2$) in the degradation of carbamazepine (CBZ) over the $CoS_x$-containing porphyra biochar catalyst was also elucidated in our recent study, following the sequential formation process: PMS $\rightarrow O_2^{\bullet-} \rightarrow {}^1O_2$ [95]. And the endogenous S species over the catalysts serve a dual role in PMS activation, functioning not only as active sites but also as the reductant that facilitates the redox cycle from Co(III) to Co(II) [95]. The ZnS/NBC catalyst, derived from porphyra biochar, demonstrated near-complete mineralization of CBZ in photothermal-synergistic PMS systems (Fig. 6C) [96]. Similar to the $CoS_x$-containing porphyra biochar catalyst, the degradation of CBZ was primarily driven by the dominant role of $^1O_2$, with additional contributions from $SO_4^{\bullet-}$, $^{\bullet}OH$, and electron transfer. As shown in the DFT results in Fig. S5C (Supporting information), the preferred atoms and abilities for electron loss and electron deficiency sites was illustrated by the HOMO and LUMO distributions of CBZ. The degradation of CBZ is mainly divided into two pathways (Fig. 6C) [96]: (1) CBZ was oxidized to generate **P2**, which then underwent a deamidation reaction to produce **P5** and **P6**. The central heterocyclic double bond of **P5** was attacked and subsequently oxidized, leading to the formation of **P8**. The simultaneous impact of $SO_4^{\bullet-}$ on **P6** resulted in subsequent carbonylation in **P9**, facilitated by the attack of $SO_4^{\bullet-}/{}^{\bullet}OH/{}^1O_2$. This process led to the elimination of the aldehyde group and generated both **P9** and $^1O_2$ for the formation of **P11**. (2) The hydroxylation of CBZ occurs *via* the attack of $^1O_2$, leading to the formation of the dihydroxy product **P3**. Subsequently, **P3** undergoes direct dehydrogenation to produce **P7**, which is further oxidized at the dihydroxy position from an aldehyde group to a carboxyl group, resulting in the formation of **P10**. The simultaneous cleavage of both C-C and N-C bonds occurs synchronously, accompanied by formylation, resulting in the generation of **P4** which can subsequently be converted into **P11**.

### 3.3. The application of electromagnetic wave absorption

With the emergence of the information age and the increasingly prominent issue of electromagnetic pollution, there has been a growing emphasis on researching high-performance materials for absorbing and responding to EMW. Biomass-derived materials, such as glucose, cellulose, and chitosan, combined with MOFs or 2D/3D layered structures, exhibit a synergistic advantage by integrating natural sustainability with tunable structural and compositional properties [20,97,98]. These materials serve as a pivotal "bridge" in functional material design, offering eco-friendliness, lightweight characteristics, and scalable fabrication.

For example, Miao *et al.* [99] utilized egg-derived porous carbon decorated with $Fe_3O_4$ nanorods *via* $SiO_2$ templating, achieving exceptional microwave absorption with a reflection loss ($RL_{min}$) of -54.19 dB at 2.46 mm and a broad effective bandwidth of 5.68 GHz through synergistic dielectric-magnetic loss mechanisms (Fig. S6A in Supporting information). Nitrogen doping further enhances performance by creating structural defects to induce polarization loss and improving conductivity. Notable examples include nitrogen-doped honeycomb carbon/Fe/$Fe_3C$ (6.5 GHz EAB at 1.85 mm) [100]

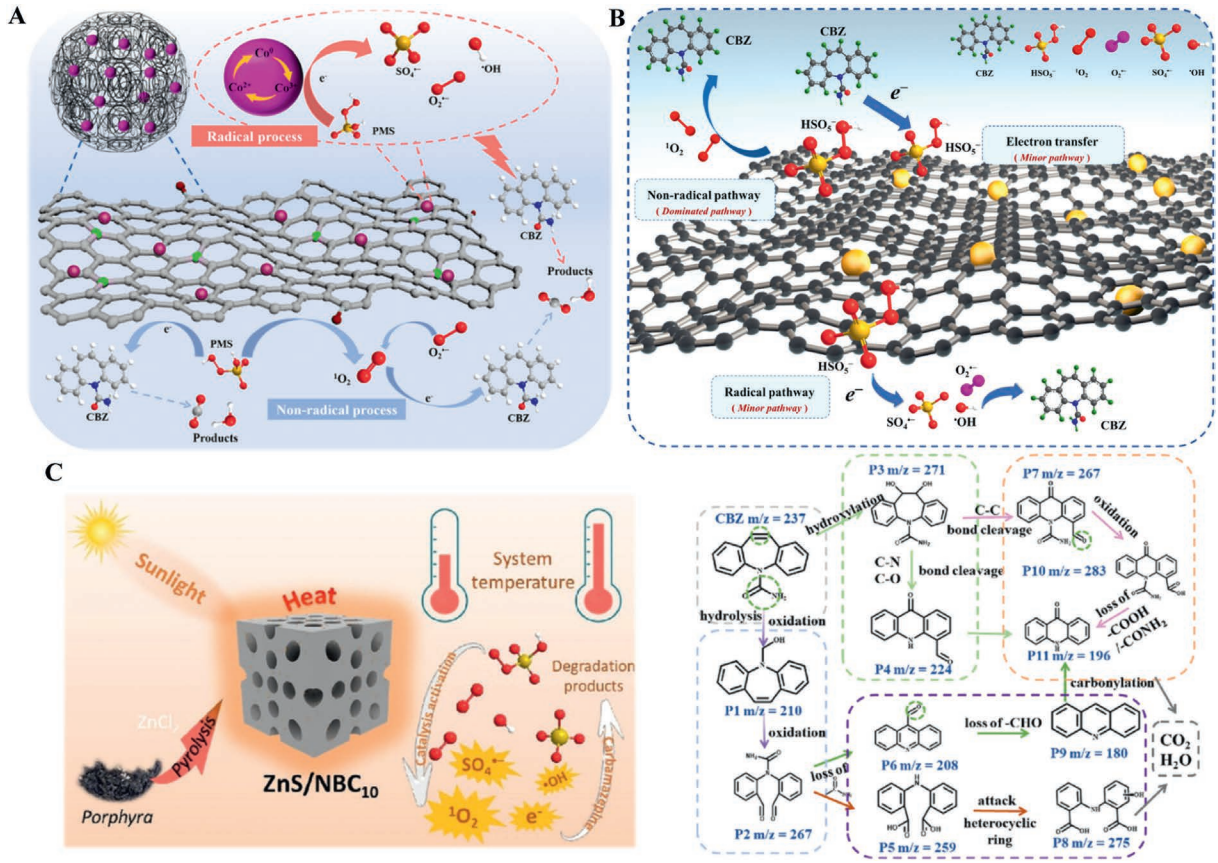



**Fig. 6.** (A) The illustration of mechanism of Co-CCF-600 for CBZ degradation. Copied with permission [26]. Copyright 2023, Elsevier. (B) The mechanism of Co-CA-900 catalysts for CBZ degradation. Copied with permission [15]. Copyright 2024, Elsevier. (C) The degradation scheme of CBZ in photothermal-synergistic PMS systems over ZnS/NBC with the potential degradation pathway. Copied with permission [96]. Copyright 2024, Elsevier.

and banana peel-derived NBCs with pyrrolic/pyridinic N (-53 dB RL) [101], where enriched N atoms optimize dielectric properties by introducing polarization centers (*e.g.*, C-N dipoles, pyridinic-N defects) and improving impedance matching, as shown in Fig. S6B (Supporting information). Lan *et al.* [102] developed a FeS/hollow C composite as a high-performance EMA material. This material achieved a $RL_{min}$ of -65 dB at 16.3 GHz with a sample thickness of 2.2 mm, and an effective absorption bandwidth (EAB) of up to 7.2 GHz at 2.6 mm thickness (Fig. S6C in Supporting information). Lin *et al.* [103] adjusted the dielectric loss and magnetic loss abilities by controlling the ratio of $Co^{2+}$ and $Zn^{2+}$ ions of the *in situ*-grown ZIF-8/ZIF-67 over the porous biomass carbon, achieving a $RL_{min}$ of -50.2 dB at 15.84 GHz as depicted in Fig. S6D (Supporting information). Ma *et al.* [104] developed a $CoFe_2O_4$@BCNPs from Apium, where the dielectric-magnetic synergy enabled ultra-wide effective absorption bandwidth (8.12 GHz) and strong RL (-58.4 dB) at low filler loading (15 wt%), while the porous architecture optimized impedance matching, offering a novel strategy for lightweight high-performance microwave absorbers. Similarly, a bamboo-derived biochar flake architecture with tunable porosity was developed by Yan *et al.* [105], which synergistically enhances electromagnetic adsorption ($RL_{min}$ = -15.8 dB, EAB = 3.8 GHz at 1.7 mm) through dielectric-conductive loss coupling and improved impedance matching, while establishing a sustainable circular economy paradigm for agroforestry waste valorization (Fig. S6E in Supporting information). Yang *et al.* [106] used coconut shell as a hierarchical carbon matrix, with evenly distributed square magnetic Fe/$Fe_3C$ cubes, achieving ultra-wide effective absorption bandwidth (7.94 GHz) and strong loss (-48.87 dB) through a simple process, offering an innovative approach for high-value utilization of biomass resources (Fig. S6F in Supporting information).

Building upon these design rationales, we precisely synthesized three-dimensional nitrogen-doped porous carbon composites (N-Ni-$Co_xS_y$/$Ni_xS_y$@C) by synergizing ZIF-67 frameworks with carboxymethyl cellulose (CMC) precursors through controlled sol-gel assembly, carbonization, and *in-situ* vulcanization techniques [107]. The carbonization of the catalysts at a temperature of 900 °C, as depicted in Fig. 7A, demonstrates that a filler mass fraction of 25 % achieves a minimum reflection loss (RL) of -48.3 dB at a frequency of 11.7 GHz. Additionally, an absorption bandwidth ranging from 13.99 GHz to 17.94 GHz is observed with a width of 3.95 GHz when the thickness is set at 1.5 mm (Fig. 7A) [107]. This Biomass/MOF composites enhance the mechanism of absorbing and mitigating electromagnetic pollution by capitalizing on the synergistic effects of interface polarization, dipole polarization, electromagnetic loss, and multiple reflection [107]. Then, the three-dimensional nitrogen-doped porous cobalt carbon/cobalt oxide (NPC/Co/CoO) composites were obtained by employing an *in-situ* growth method to transform ZIF-67 clusters onto a chitosan matrix, affording the catalysts with remarkable electromagnetic pollution absorbance, effectively covering the entire X-band [108]. The carbon matrix and Co/$CoO_x$ species possess a significant number of electron/hole-free carriers, thereby facilitating the migration and hopping of electrons stimulated by alternating electromagnetic and porous structures between Co/$CoO_x$ nanoparticles, and the carbon matrix enhances interfacial polarization [108]. Finally, the magnetic coupling between adjacent magnetic particles hinders the propagation of incident EMW within the catalyst and enhances its ability to attenuate them [108].

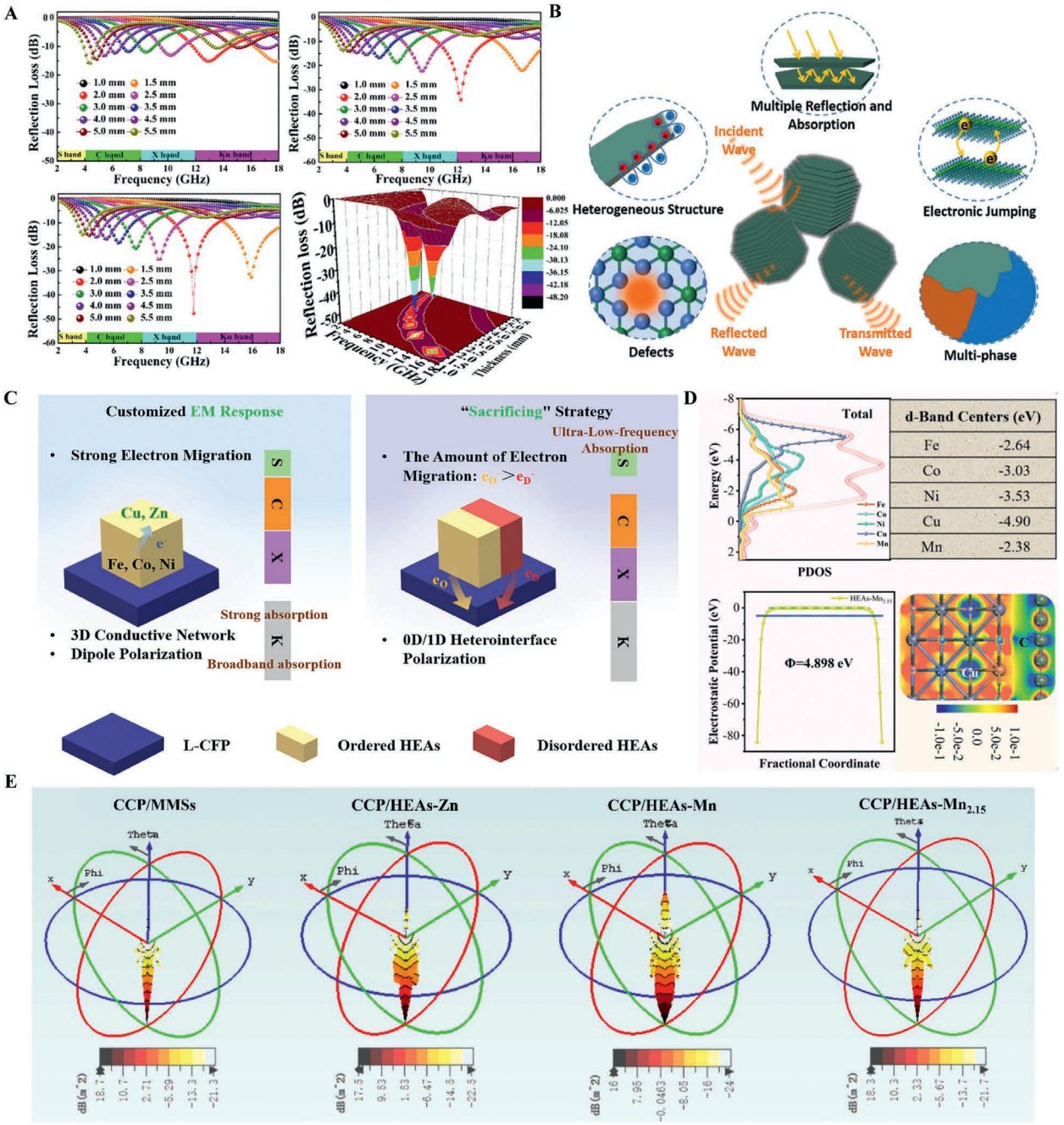



**Fig. 7.** (A) EMW absorbance performance of N-Ni-$Co_xS_y$/$Ni_xS_y$@C catalysts. Copied with permission [107]. Copyright 2021, Elsevier. (B) EMW absorption mechanisms in the $VS_2$/GDC catalyst. Copied with permission [25]. Copyright 2023, Elsevier. (C) Absorbing mechanism of the L-CFP/FeCoNiCuZn-X. Copied with permission [48]. Copyright 2024, Wiley. (D) The electronic properties, EMW absorbance performance, and (E) 3D RCS plots of CCP/HEAs-$Mn_{2.15}$. Copied with permission [49]. Copyright 2024, CC BY-NC-ND 4.0.

The efficient utilization of $VS_2$ is impeded by the technical bottleneck of its narrow effective absorption bandwidth in the domain of EMW absorption [25]. To overcome this limitation, a facile hydrothermal method was employed for the surface decoration of stacked $VS_2$ nanosheets with biomass-derived glucose carbon (GDC), followed by subsequent high-temperature carbonization. The $VS_2$/GDC hybrids demonstrated a remarkable minimum $RL_{min}$ of 52.8 dB at a frequency of 12.2 GHz, with a thickness of 2.7 mm [25]. Interestingly, in comparison to pristine $VS_2$, the hybrids demonstrated an expanded effective absorption bandwidth (EAB) ranging from 2.0 to 5.7 GHz, while their environmental stability was significantly enhanced through GDC doping. As shown in Fig. 7B, the notably EMW absorption performance of $VS_2$/GDC hybrids can be attributed to the synergistic effect of conductive loss coupling, interfacial polarization, relaxation, dipole polarization, defect engineering, and multiple reflections and absorptions [25].

The carbon thermal shock method enables the construction of composite materials with heterogeneous interfaces between high entropy alloys (HEAs) and biomass, showcasing remarkable potential in terms of EMW absorption efficiency. The FeCoNiCuZn catalyst establishes a heterogeneous interface between 0D and 1D, playing a crucial role in achieving broadband and high-intensity EMW absorption performance [48]. As a result, the absorption capabilities of ultra-low frequency EMW are effectively enhanced, resulting in a significantly low reflection loss of -49.1 dB achieved at

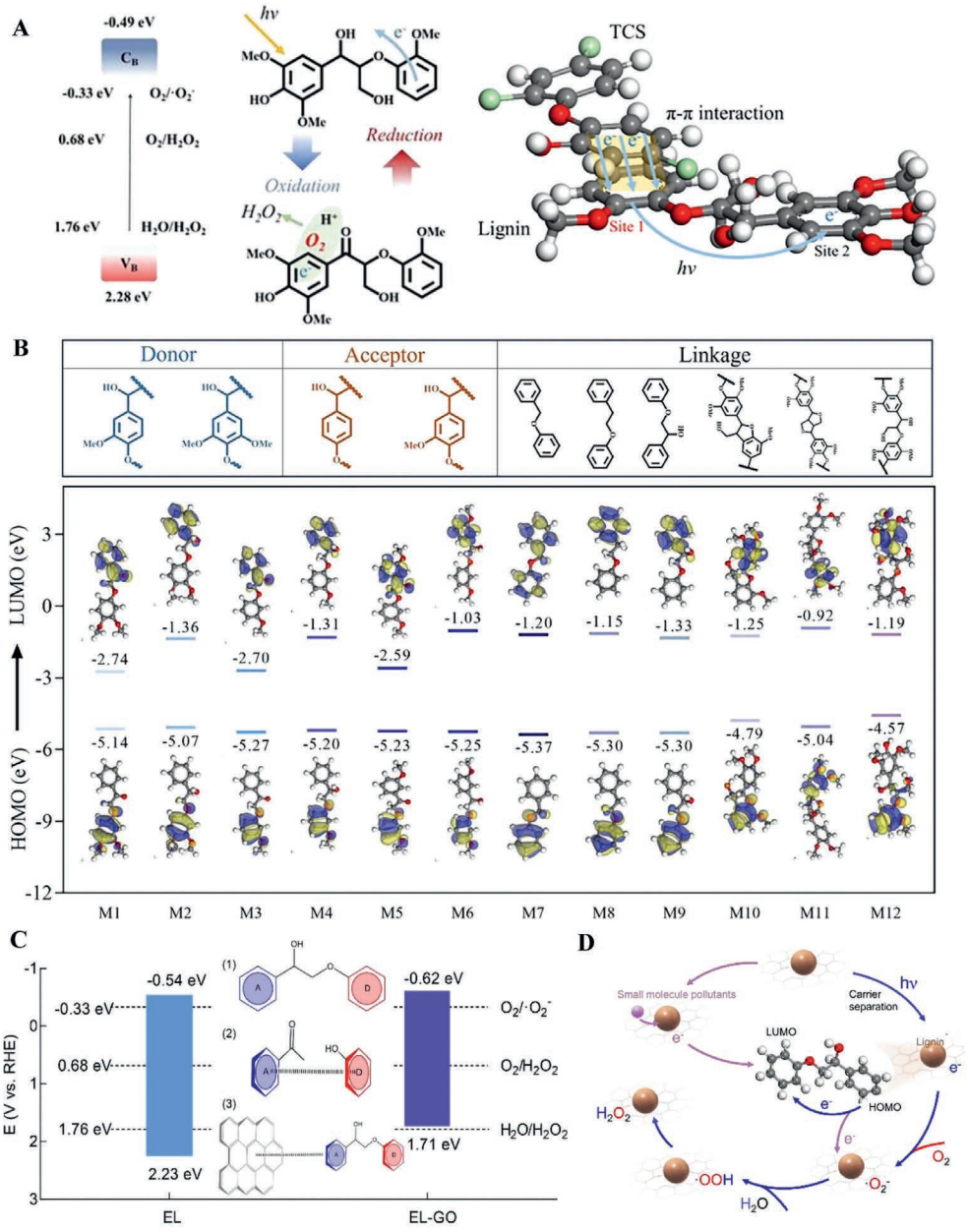



**Fig. 8.** (A) The energy level structure diagram of EL and the working mechanism of $H_2O_2$ production and photocatalytic $H_2O_2$ production assisted by TCS. (B) The corresponding HOMO and LUMO energy levels. (A, B) Copied with permission [109]. Copyright 2024, Elsevier. (C) Energy level structure of EL and EL-GO. (D) The possible mechanism of EL-GO photocatalytic $H_2O_2$ production. (C, D) Copied with permission [110]. Copyright 2025, CC BY-NC-ND 4.0.

3.2 GHz, accompanied by over 50 % effective absorption bandwidth coverage within the 2-4 GHz frequency range [48]. The L-CFP/semi-disordered HEAs heterogeneous interface, constructed using the "sacrifice" strategy as shown in Fig. 7C, selectively compromises polarization relaxation in the low frequency range while maintaining high attenuation capacity, facilitating the co-optimization of conductive and relaxation losses [48]. The migration of electrons in high entropy alloys and at heterogeneous interfaces is primarily influenced by the Cu and Zn elements, which significantly contribute to dielectric loss. Additionally, local charge redistribution induced by polar functional groups, strong local electron migration facilitated by electron negative difference between different elements, and impedance matching modulation through electron transfer at the heterogeneous interface play important roles.

In our recent work, the electron migration mode of CCP/HEAs-$Mn_{2.15}$ is effectively preserved to the maximum extent through an enhanced carbon thermal shock process, ensuring the retention of a switchable electron-rich site (Fig. 7D) [49]. The dipole polarization efficiency of HEAs-$Mn_{2.15}$ is greatly improved as the molar ratio of Mn increases, leading to a highly effective EMW absorption capability (-51.35 dB) for the CCP/HEAs-$Mn_{2.15}$ composite at an ultra-thin matching thickness of 1.03 mm [49]. The radar (Fig. 7E) cross sections of four target samples are simulated using electromagnetic simulation technology to efficiently absorb electromagnetic signals at various optimal matching thicknesses and validate the effective coupling of diverse elements in their response [49]. The RCS simulation shows that each sample has distinct RCS attenuation values at corresponding thicknesses, and CCP/HEAs-$Mn_{2.15}$ demonstrates effective EMW absorption even at very thin thicknesses. Importantly, the unique heterogeneous interface structure enables highly efficient EMW absorption at an ultra-thin thickness, while the differential conductivity promotes interface polarization

and the formation of energy equivalent dipoles in HEAs-$Mn_{2.15}$, enhancing its dielectric properties.

### 3.4. Other applications

In addition to the mentioned applications of adsorption, wave absorption, and pollutant degradation, biomass-based functional materials are also used for energy storage in supercapacitors and extensively applied in photocatalytic conversion. The focus of this review is primarily on the utilization of biomass-derived materials in the production of photocatalytic $H_2O_2$.

The lignin photocatalyst series, obtained *via* ethanol pulping method, is capable of undergoing reduction in the presence of light and $O_2$ to generate $H_2O_2$. As illustrated in Fig. 8A, the presence of $\beta$-O-4 ether bonds allows for minimal overlap between the adjacent benzene rings, thereby segregating them into distinct HOMO and LUMO energy levels [109]. Additionally, the HOMO level is jump to the LUMO level with the aid of TCS *via* $\pi$-$\pi$ interactions, thereby facilitating electron transfer and contributing to the generation of $H_2O_2$ [109]. Furthermore, the stability of lignin's structure is maintained during photocatalysis due to the electron-donating and accepting properties of $\beta$-O-4 ether bonds, effectively minimizing the possibility of internal structural degradation caused by reactive species. The conjugation between methoxy and benzene enhances the electron-donating capacity of the highest occupied HOMO, while the induction between hydroxyl or carbonyl groups and carbon improves the electron-accepting capacity of LUMO (Fig. 8B) [109].

After that, a lignin nanosphere-GO composite (EL-GO) was synthesized *via* self-assembled method to produce the $H_2O_2$ through the photoelectron migration modes. The free electrons in GO occupy the previously designated sites for displaced photoelectrons at the LUMO energy level, leading to an almost fully saturated electronic state of the valence band over the catalyst and further causing EL-GO to lose its oxidation activity (Fig. 8C) [110]. This electron migration mode facilitates the utilization of visible light and stimulate surface electron activity, thereby enhancing overall efficiency. In detail, the retained $\beta$-O-4 ether bonds, accounting for 63.5 % of the total content (Fig. S7A in Supporting information), possess the potential to function as sites for photoelectron excitation and separation, as well as play a pivotal role in lignin's photo-responsive activity (Fig. S7B in Supporting information). Besides, the electron transfer effect between GO and EL over the catalyst facilitates the formation of an electron-rich region in the lower potential GO, thereby promoting the unidirectional flow of electrons from EL to GO (Fig. S7C in Supporting information) [110]. And the recombination time of photoelectrons is consequently prolonged, thereby making a contribution to the production of $H_2O_2$. Finally, we proposed the EL-GO photocatalytic $H_2O_2$ production mechanism (Fig. 8D) [110]: (1) The photoelectric transition is induced by the irradiation of light, causing the EL-GO to undergo a transition from the HOMO to the LUMO energy level. (2) The $\pi$-$\pi$ interaction between the "donor site" and the "acceptor site" functional region, along with the oriental migration of photoelectrons between GO and EL, effectively extends the recombination lifetime of photoexcited electrons. (3) The photocatalyst EL-GO facilitates the gradual conversion of $O_2$ to $H_2O_2$ under illuminated conditions.

## 4. Conclusions and outlook

The utilization of biomass-derived multifunctional materials plays a pivotal role in the remediation of environmental pollutants and the storage of energy, have garnered increasing attention. In this review, we summarized our strategies encompassing mesoscopic morphology control, electronic modification, and molecular self-assembly, employed for the fabrication of metal-carbon materials derived from biomass, and further elucidated the intrinsic mechanism underlying the formation of the specific microstructure of the catalyst. These multifunctional catalysts endowed remarkable catalytic performance in the aspects of heavy metal ion adsorption in wastewater, antibiotic contaminant degradation, EMW absorption, and $O_2$ catalytic conversion to $H_2O_2$. Moreover, we also unveiled the adsorption mechanism, degradative pathway, and proposed reaction mechanism of biomass-derived multifunctional materials during their detailed application process. However, the investigation of the activation of peroxides/EMW and the decomposition of pollutants is still in its preliminary stage, necessitating advanced *in situ/operando* characterization techniques and reliable experimental design. The following aspects warrant greater attention and dedication.

The future research should prioritize the synthesis of functional carbon materials derived from biomass, utilizing renewable biomass resources to design catalysts with diverse microstructure and properties through precise control over their type, morphology, and dimensions, aiming to expand the application of biomass-based functional carbon materials in traditional catalytic domains such as chemical catalysis and electrocatalysis, while actively expanding their application in other fields.

In view of the diverse composition of metal/carbon heterostructures offers significant opportunities for tailoring electronic properties (valence state, spin state, geometrical configuration, *etc.*) and active sites, thereby enabling the realization of unique heterostructures that exhibit remarkable catalytic performance in heterogeneous catalysis. The fabrication of metal/carbon heterostructures can be achieved through an *in-situ* synthesis strategy employing CuS, $TiO_2$, and $MoS_2$. Importantly, due to the high N and C contents of the biomass, which are also abundant in heteroatoms and easily modifiable in terms of structure, it is possible to construct single/dual-atom catalysts (SACs/DACs) as the model for investigating their catalytic mechanism in adsorption and activation during pollution degradation.

Further delve into the "structure-function" relationship between biomass-derived carbon materials, it is anticipated that *in situ* and *operando* hyperfine structure and spectral analysis techniques (such as Mössbauer, XAS, EPR, Raman spectroscopy) will provide insights into the catalytic mechanism. Besides, within the realm of computer science, the discipline of machine learning utilizes a data-centric methodology to facilitate computers in acquiring knowledge from generated datasets, conducting analysis, making programmed-based predictions, and attaining profound understandings regarding the complex interplay between material composition and characteristics. By analyzing extensive datasets of material properties and structures, the utilization of machine learning models can effectively guide the optimization of catalytic performance and provide innovative insights for catalyst design, selection, and elucidation of catalytic mechanisms. Furthermore, artificial intelligence (AI) can simulate and optimize the synthesis processes of these materials, potentially reducing production costs and environmental impact while maintaining or improving quality. This can facilitate the scale-up and industrialization of biomass-derived materials, bridging the gap between laboratory research and practical applications. The combination of machine learning and experimental approaches can accelerate the development of high-performance biomass-derived materials, contributing to a more sustainable and resource-efficient future.

## Declaration of competing interest

The authors declare that they have no known competing financial interests or personal relationships that could have appeared to influence the work reported in this paper.

## CRediT authorship contribution statement

**Yujia Zhao:** Writing – original draft, Resources, Formal analysis, Conceptualization. **Yingyi Li:** Writing – original draft, Investigation, Formal analysis, Conceptualization. **Qingda An:** Supervision, Formal analysis, Conceptualization. **Shuang Shan:** Writing – original draft, Conceptualization. **Xianquan Li:** Writing – review & editing, Visualization, Supervision, Conceptualization. **Shangru Zhai:** Writing – review & editing, Visualization, Supervision, Funding acquisition, Conceptualization.

## Acknowledgment

This work was supported by the National Natural Science Foundation of China (Nos. 21776026, 22075034, 22178037, U22A20424, and 22502191).

## Supplementary materials

Supplementary material associated with this article can be found, in the online version, at doi:10.1016/j.cclet.2025.112357.

## References

[1] Z. Zhu, S. Zhong, C. Cheng, et al., Chem. Rev. 124 (2024) 11348–11434.
[2] L. Zhang, B. Zhang, G. Xia, X. Li, J. Wang, Acc. Mater. Res. 5 (2024) 585–599.
[3] W. Li, L. Zhu, Y. Xu, et al., Adv. Mater. 37 (2024) 2415761.
[4] C. Wang, W. Zhang, X. Qiu, C. Xu, EnergyChem 6 (2024) 100133.
[5] W. Yang, W. Yang, J. Zeng, et al., Pro. Mater. Sci. 144 (2024) 101264.
[6] Y. Zhang, G. Yang, J. Wang, et al., EES Catal. 2 (2024) 475–506.
[7] B. Zhang, M. Zhao, K. Cheng, et al., Coord. Chem. Rev. 523 (2025) 216234.
[8] R. Peng, R. Xin, D. Wu, et al., Chem. Eng. J. 497 (2024) 154908.
[9] B. Yuan, Q. An, Z. Xiao, et al., Resour. Chem. Mater. 2 (2023) 231–244.
[10] H. Wang, Q. An, Z. Xiao, et al., J. Mater. Chem. A 10 (2022) 17023–17052.
[11] C. Bie, H. Yu, B. Cheng, et al., Adv. Mater. 33 (2021) 2003521.
[12] X. Zhao, Q.D. An, Z.Y. Xiao, S.R. Zhai, Z. Shi, Chin. J. Catal. 39 (2018) 1842–1853.
[13] H. Lv, Z. Xiao, S. Zhai, et al., Ind. Crop. Prod. 194 (2023) 116320.
[14] Y. Qin, X. Li, L. Wang, et al., Sep. Purif. Technol. 281 (2022) 119901.
[15] C. Yao, Y. Qin, Y. Li, et al., Sep. Purif. Technol. 307 (2023) 122728.
[16] J. Lv, S. Zhai, Y. Fan, Z. Lei, Q. An, J. Taiwan Inst. Chem. Eng. 62 (2016) 209–218.
[17] X. Zhang, C. Chen, C. Tang, Y. Wang, Acc. Mater. Res. 3 (2022) 525–539.
[18] C. Huang, Y. Zhai, Chemosphere 362 (2024) 142775.
[19] Y. Wang, Y. Liu, H. Zhang, et al., Chem. Soc. Rev. 54 (2025) 2436–2482.
[20] Z. Mu, P. Xie, D.A. Alshammari, et al., Adv. Compos. Hybrid Mater. 7 (2024) 220.
[21] B. Mao, Q. An, B. Zhai, Z. Xiao, S. Zhai, RSC Adv. 6 (2016) 47761–47770.
[22] S. Gao, Q. An, Z. Xiao, S. Zhai, D. Yang, ACS Appl. Nano Mater. 1 (2018) 5895–5906.
[23] S. Bo, J. Luo, Q. An, et al., J. Clean. Prod. 236 (2019) 117630.
[24] L. Gai, Q. An, Z. Xiao, et al., Micropor. Mesopor. Mater. 294 (2020) 109880.
[25] H. Wang, H. Zhang, J. Cheng, et al., J. Materiomics 9 (2023) 492–501.
[26] Y. Li, Q. An, Z. Xiao, et al., Chem. Eng. J. 487 (2024) 150636.
[27] X. Shan, X. Zhou, W. Cui, et al., ACS Appl. Nano Mater. 7 (2024) 22177–22188.
[28] Q. Yu, J. Zhou, W. Wang, et al., Microchim. Acta 192 (2025) 84.
[29] S. Wang, Y. Huang, S. Ma, et al., Biochar 5 (2023) 24.
[30] Y. He, J. Wang, L. Lei, et al., J. Environ. Chem. Eng. 12 (2024) 113743.
[31] H. Zhu, Y. Wu, H. Chen, et al., Biomass Bioenerg 191 (2024) 107470.
[32] X. Yang, H. Wang, J. Chen, et al., Int. J. Miner. Metall. Mater. 31 (2024) 812–824.
[33] Z. Jiang, X. He, K. Zhu, et al., Desalination 592 (2024) 118085.
[34] X. Wang, X. Cao, E. Ding, et al., Carbon 221 (2024) 118887.
[35] X. Li, H. Zhou, J. Zhang, et al., J. Mater. Chem. A 12 (2024) 4057–4066.
[36] A. Ni, Z. Xiong, Y. Zhang, et al., Carbon 221 (2024) 118930.
[37] S. Bo, J. Luo, Q. An, et al., J. Clean. Prod. 250 (2020) 119585.
[38] J. Luo, S. Bo, Q. An, et al., Micropor. Mesopor. Mater. 293 (2020) 109810.
[39] Y. Qin, J. Luo, Q. An, et al., Micropor. Mesopor. Mater. 323 (2021) 111259.
[40] Z. Li, C. Yu, Structure–performance relationship of nanomaterials, in: Z. Li, C. Yu (Eds.), Nanostructured Materials, Elsevier, 2024, pp. 43–92.
[41] F. Ye, W. Sun, K. Pang, et al., Chin. Chem. Lett. 34 (2023) 107755.
[42] G. Song, L. Gai, K. Yang, et al., Carbon 181 (2021) 335–347.
[43] R. Tang, D. Gong, Y. Deng, et al., J. Hazard. Mater. 423 (2022) 126944.
[44] Z. Guo, P. Ren, F. Zhang, et al., J. Colloid Interface Sci. 610 (2022) 1077–1087.
[45] X. Wang, H. Wu, J. Jing, et al., Green Energy Environ. 10 (2025) 214–230.
[46] H. Lv, Z. Xiao, S. Zhai, et al., J. Alloys Compd. 945 (2023) 169332.
[47] R. Tan, Y. Liu, W. Li, et al., Small Methods 8 (2024) 2301772.
[48] H. Wang, X. Xiao, Q. An, et al., Small 20 (2024) 2309773.
[49] H. Wang, X. Xiao, S. Zhai, et al., Nano-Micro Lett. 17 (2024) 19.
[50] H. Li, J. Liu, Y. Wang, et al., Coord. Chem. Rev. 523 (2025) 216240.
[51] H. Wang, Q. Chen, H. Xia, R. Liu, Y. Zhang, Sep. Purif. Technol. 328 (2024) 125074.
[52] X. Qi, H. Yin, M. Zhu, et al., Chemosphere 294 (2022) 133733.
[53] Y. Zhao, X. Shan, Q. An, Z. Xiao, S. Zhai, Chem. Eng. J. 398 (2020) 125561.
[54] J. Luo, S. Bo, Y. Qin, et al., Chem. Eng. J. 395 (2020) 125063.
[55] Y. Li, L. Gai, G. Song, et al., Carbon 186 (2022) 238–252.
[56] L. Gai, Y. Zhao, G. Song, et al., Compos. Part A: Appl. Sci. Manuf. 136 (2020) 105965.
[57] K. Abhishek, A. Shrivastava, V. Vimal, et al., Sci. Total Environ. 853 (2022) 158562.
[58] A.T. Hoang, S. Nižetić, C.K. Cheng, et al., Chemosphere 287 (2022) 131959.
[59] P.S. Kumar, R. Gayathri, B.S. Rathi, Chemosphere 285 (2021) 131438.
[60] Y. Trivedi, M. Sharma, R.K. Mishra, et al., Desalination 600 (2025) 118509.
[61] H. Hinsene, N. Bhawawet, A. Imyim, Sep. Purif. Technol. 339 (2024) 126638.
[62] P. Hao, H. Fu, S. Ma, et al., Sep. Purif. Technol. 363 (2025) 132079.
[63] J. Tian, X. Li, W. Ding, et al., Chem. Eng. J. 508 (2025) 161178.
[64] Y. Zhang, B. Mei, B. Shen, et al., Carbohydr. Polym. 312 (2023) 120834.
[65] X. Fan, X. Wang, Y. Cai, et al., J. Hazard. Mater. 423 (2022) 127191.
[66] X. Shan, Y. Zhao, S. Bo, et al., Sci. Total Environ. 796 (2021) 148984.
[67] S. Li, X. Wang, Q. An, et al., Int. J. Biol. Macromol. 143 (2020) 640–650.
[68] W. Zheng, Q. An, Z. Lei, et al., RSC. Adv. 6 (2016) 104897–104910.
[69] Y. Zhang, Y. Jiang, Y. Qin, et al., Colloids Surf. A: Physicochem. Eng. Aspects 643 (2022) 128790.
[70] Y. Zhang, Q. An, Z. Xiao, et al., Int. J. Biol. Macromol. 253 (2023) 127368.
[71] Z. Guo, C. Zhao, L. Meng, et al., Appl. Catal. B: Environ. 377 (2025) 125507.
[72] S. Ahmad, L. Liu, S. Zhang, J. Tang, J. Hazard. Mater. 446 (2023) 130727.
[73] J. Dou, J. Cheng, Z. Lu, et al., Appl. Catal. B: Environ. 301 (2022) 120832.
[74] S. Qu, Y. Yuan, X. Yang, et al., Chem. Eng. J. 441 (2022) 135864.
[75] L. Li, J. Zhao, X. Zhao, Z. Zhou, G. Jing, Sep. Purif. Technol. 354 (2025) 129005.
[76] L. Du, D. Huang, M. Cheng, et al., Chem. Eng. J. 504 (2025) 158889.
[77] P. Huang, P. Zhang, C. Wang, J. Tang, H. Sun, Appl. Catal. B: Environ. 303 (2022) 120926.
[78] L. Xu, Z. He, X. Wei, et al., Chem. Eng. J. 461 (2023) 142028.
[79] Z. Liu, X. Shi, Z. Yan, Z. Sun, Bioresour. Technol. 406 (2024) 130983.
[80] J. Lu, Q. Lu, L. Di, Y. Zhou, Y. Zhou, Chin. Chem. Lett. 34 (2023) 108357.
[81] D. Cheng, Y. Feng, B. Feng, et al., Chin. Chem. Lett. 35 (2024) 108623.
[82] H. Zhu, A. Guo, S. Wang, et al., Chem. Eng. J. 450 (2022) 138428.
[83] C. Zhang, R. Pan, H. Wang, et al., J. Colloid Interface Sci. 670 (2024) 50–60.
[84] D. Ma, Y. Yang, B. Liu, et al., Chem. Eng. J. 408 (2021) 127992.
[85] Y. Liu, T. Wang, Q. Hong, et al., J. Hazard. Mater. 477 (2024) 135343.
[86] X. Wang, W. Li, J. Zhang, et al., Chem. Eng. J. 491 (2024) 151915.
[87] X. Zhao, Q. An, Z. Xiao, S. Zhai, Z. Shi, Chem. Eng. J. 353 (2018) 746–759.
[88] S. Bo, X. Zhao, Q. An, et al., RSC Adv. 9 (2019) 5009–5024.
[89] S. Liu, H. Fu, F. Wang, et al., Appl. Catal. B: Environ. 346 (2024) 123753.
[90] F. Wang, Y. Gao, H. Fu, et al., Appl. Catal. B: Environ. 339 (2023) 123178.
[91] Y. Wei, H. Fu, C. Zhao, et al., Appl. Catal. B: Environ. 372 (2025) 125290.
[92] F. Wang, Y. Gao, Y. Chai, et al., Appl. Catal. B: Environ. 364 (2025) 124848.
[93] L. Meng, Y. Li, C. Zhao, et al., Appl. Catal. B: Environ. 377 (2025) 125521.
[94] F. Sun, X. Yang, F. Shao, et al., Chin. Chem. Lett. 34 (2023) 108563.
[95] X. Peng, Y. Li, K. Zhu, et al., J. Environ. Chem. Eng. 11 (2023) 110988.
[96] X. Peng, Y. Li, Z. Jiang, et al., Chem. Eng. J. 489 (2024) 151263.
[97] Z. Jiao, M. Ma, Y. Bi, et al., J. Mater. Sci. 57 (2022) 18243–18265.
[98] S. Sharma, S. Parne, S. Panda, S. Gandi, Adv. Colloid Interface Sci. 327 (2024) 103143.
[99] Y. Miao, M. Zhang, Q. Liu, et al., Carbon 235 (2025) 120076.
[100] Y. Wang, H. Han, H. Bian, Y. Li, Z. Lou, Int. J. Miner. Metall. Mater. 32 (2025) 631–644.
[101] Y. Lu, X. Zhao, Q. Tian, et al., Carbon 224 (2024) 119083.
[102] X. Lan, R. Wang, W. Liu, et al., Chem. Eng. J. 485 (2024) 149238.
[103] X. Lin, Y. Zhou, J. Hong, et al., Chin. Chem. Lett. 35 (2024) 109835.
[104] G. Ma, D. Lan, Y. Zhang, et al., Small. 20 (2024) 2404449.
[105] H. Yan, Z. Lou, L. Xu, H. Lv, Chem. Eng. J. 464 (2023) 142568.
[106] S. Yang, X. Sun, S. Wang, et al., Carbon 196 (2022) 354–364.
[107] G. Song, K. Yang, L. Gai, et al., Compos. Part A: Appl. Sci. Manuf. 149 (2021) 106584.
[108] K. Yang, G. Song, Y. Li, et al., J. Alloys Compd. 936 (2023) 168195.
[109] X. Xiao, H. Wang, X. Wang, et al., Chem. Eng. J. 494 (2024) 153151.
[110] X. Xiao, H. Wang, X. Wang, et al., Carbon Energy 7 (2025) e666.